Materials Advances

ROYAL SOCIETY OF CHEMISTRY

PAPER

View Article Online
View Journal | View Issue

Cite this: *Mater. Adv.*, 2026, 7, 3373

Self-assembled α/β-dipeptides as dielectrics to improve the behavior of multilayered conducting polymer pseudocapacitors

Dulce A. Quintana-Romero,[ab] Adrián Fontana-Escartín,*[ac] Maria Luisa Gelmi,*[c] Merve Gul,[ac] Maria M. Pérez-Madrigal,[ac] Raffaella Bucci*[b] and Carlos Alemán*[acd]

Multilayered films composed of two different materials, where the less conducting one acts as a dielectric separating the layers made of the other, are known to function as efficient electrodes for electrochemical supercapacitors. In this work, we extend this concept, which was previously applied only to soft supercapacitors made from two or more conducting polymers with markedly different electrochemical activities, to examine for the first time the utilization of α/β-dipeptides in conducting polymer electrodes for symmetric supercapacitors. Specifically, we investigate the α/β-dipeptides formed by L-alanine and *syn*-3-amino-2-(2-fluorophenyl)-3-phenylpropanoic acid in two forms: (1) an α/β-dipeptide with $-NH_2$ as the free terminal amino group; and (2) an α/β-dipeptide with a protonated amino group stabilized through an ionic pair with trifluoroacetate (**TFA·DP1**). After examining the self-assembly of **DP1** and **TFA·DP1** on electropolymerized poly(3,4-ethylenedioxythiophene) (PEDOT) films, we fabricated three-layered electrodes consisting of two PEDOT layers separated by an intermediate layer of self-assembled **DP1** or **TFA·DP1**, and subsequently characterized them. The best electrochemical response was achieved with the **TFA·DP1**-containing three-layered electrodes. These electrodes were then used to assemble symmetric supercapacitors, which were characterized by cyclic voltammetry, galvanostatic charge–discharge analysis and electrochemical impedance spectroscopy. The specific capacitance of devices incorporating **TFA·DP1** between submicrometric PEDOT layers, which performed better than those in which the self-assembled peptide was omitted, was around 47 mF cm^{-2}. In these optimized devices, the intermediate TFA-**DP1** assemblies act as ultrathin, randomly distributed dielectrics connected in series with one another and in parallel with the PEDOT layers.

Received 11th October 2025,
Accepted 4th December 2025

DOI: 10.1039/d5ma01170a

rsc.li/materials-advances

Introduction

Over the past fifteen years, significant efforts have been made to develop soft electrochemical energy storage devices, such as batteries and supercapacitors (SCs), in a simple and cost-effective manner.[1–4] SCs are considered efficient electrochemical energy storage devices for power drifting applications due to their excellent power density, moderate energy density, ultrafast charge/discharge rates and long cycle life.[5–7] Based on the type of charge storage exhibited by the SC electrodes, SCs are classified into three types:[8,9] (1) electrochemical double layer capacitors (EDLCs), which store charge *via* a charge–discharge process (electro-sorption) in an electric double layer on porous electrodes (*e.g.* activated carbons and carbon nanotubes); (2) pseudocapacitors, which store charge by reversible faradaic redox reactions (*e.g.* transition metal oxides and electronically conducting polymers); and (3) battery-type hybrid capacitors, which combine the benefits of an EDLC and a pseudocapacitor to provide higher energy and power densities.

Among the conjugated conducting polymers used to fabricate electrochemical pseudocapacitors, poly(3,4-ethylenedioxythiophene) (PEDOT) has been extensively employed. This is due to its excellent pseudocapacitance, which derives from the following features: its superior ionic charge mobility, outstanding electrical conductivity, fast and reversible redox reactions coupled with doping/de-doping processes, exceptional thermal

[a] *IMEM-BRT Group, Departament d'Enginyeria Química, EEBE, Universitat Politècnica de Catalunya. BarcelonaTech (UPC), Av. Eduard Maristany, 16, Barcelona 08019, Spain. E-mail: adrian.fontana@upc.edu, carlos.alema@upc.edu*
[b] *Department of Pharmaceutical Sciences, University of Milan, via Venezian 21, Milano 20133, Italy. E-mail: raffaella.bucci@unimi.it*
[c] *Barcelona Research Centre in Multiscale Science and Engineering (CCEM), Universitat Politècnica de Catalunya. BarcelonaTech (UPC), Av. Eduard Maristany, 16, Barcelona 08019, Spain. E-mail: marialuisa.gelmi@unimi.it*
[d] *Institute for Bioengineering of Catalonia (IBEC), The Barcelona Institute of Science and Technology, Baldiri Reixac 10-12, 08028 Barcelona, Spain*

and chemical stability, and resilience to expansion and contraction during electrochemical reactions.[10–14] Indeed, PEDOT is frequently used in combination with other electrochemically active materials (*e.g.* clays,[15,16] other conducting polymers,[17,18] graphene,[19,20] and MXenes[21,22]) to obtain effective hybrid and composite electrodes. The engineering of these complex electrodes involves the underlying use and sometimes even the explicit search for synergy between the materials being combined.[23]

On the other hand, peptide-based materials, which are exploited for their ability to self-assemble into well-shaped three-dimensional micro- and nanostructures, offer a variety of potential applications in environmentally friendly energy storage technologies. Thus, different α-peptide materials have been used to fabricate SCs taking advantage of the versatility of peptide sequences and various peptide self-assembly pathways.[24–32] Due to the difficulties in the scalability of their synthesis, peptides are usually combined with other materials, forming hybrid or multilayered composite materials. For example, Hu *et al.*[32] sandwiched Fmoc-Glu-Phe-NH_2 dipeptide fibers coated with a TiO_2 layer and a polyvinyl alcohol (PVA)/H_3PO_4 gel electrolyte between two polyethylene terephthalate (PET) films to obtain an outstanding areal capacitance of 8.6 mF cm^{-2}.

In this work, we go one step forward investigating for the first time the utilization of α/β-dipeptides in electrodes for pseudocapacitors. More specifically, we have considered dipeptides involving L-alanine (L-Ala) and *syn*-3-amino-2-(2-fluorophenyl)-3-phenylpropanoic acid (β-Fpg), which are expected to exhibit well-shaped self-assemblies due to the aromatic aryl groups, the lipophilic fluorine atom, and the extended conformation typically driven by *syn*-$\beta^{2,3}$-amino acids.[33,34] Indeed, the protected α/β-dipeptide Boc-L-Ala-β-2*S*,3*S*-Fpg-OMe was reported to self-assemble into well-defined nanotubes stabilized by intermolecular hydrogen bonds, π–π stacking, as well as C_π–H···O and C_π–H···F interactions.[35] Moreover, when the same dipeptide is further functionalized with a cationic construct the same interactions promote the formation of spherical structures.[36] More recently, we also investigated the electrochemical behavior of peptidomimetics incorporating the β-2*S*,3*S*-Fpg residue. Our findings highlighted the importance of forming highly ordered nanomaterials, which were drop-cast onto PEDOT substrates to enhance electrochemical performance.[37] In order to enhance the self-assembly capacity and the electrochemical response, both the formation of intermolecular electrostatic interactions and ionic transport have been promoted by selecting both the

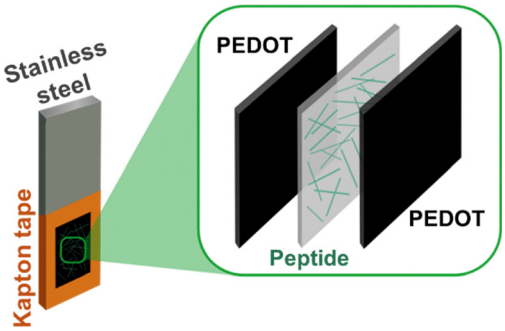

Scheme 2 Sketch of the three-layered electrodes prepared in this work.

N-unprotected dipeptide (**DP1** in Scheme 1) and the corresponding peptide protonated at the terminal amino group stabilized by forming an ionic pair with trifluoroacetate (**TFA·DP1** in Scheme 1). Accordingly, the charge transport in the protonated peptide is expected to arise not only from the electron transfer flowing through stacked aromatic rings of β-2*S*,3*S*-Fpg, like in the neutral peptide, but also from the proton and/or counterion transport.

More specifically, herein, we present multilayer composite electrodes for pseudocapacitors that have been obtained by promoting the self-assembly of **DP1** and **TFA·DP1** between two anodically polymerized PEDOT films (Scheme 2). For this purpose, the self-assembly of the peptides, which have been drop cast on the surface of a PEDOT substrate, has been investigated considering not only the conditions used to dissolve the peptides (*i.e.* solvent mixtures and concentrations) but also the roughness of the PEDOT film. In this work, the roughness of PEDOT films has been tuned by varying the polymerization time (t_p), which also affects the film thickness. The resulting peptide-coated PEDOT films (PEDOT(#) + **DP1** and PEDOT(#) + **TFA·DP1**, where # refers to t_p) have been covered by adding another layer of anodically polymerized PEDOT, which has been prepared using a t_p identical to that of the first layer. Hereafter, the resulting 3-layered electrodes have been denoted 2PEDOT(#)-**DP1** and 2PEDOT(#)-**TFA·DP1**. After evaluating the electrochemical behavior of the fabricated electrodes, those with better properties have been selected as electrodes for constructing SCs. The performance and stability of such devices have been analyzed by cyclic voltammetry (CV), galvanostatic charge–discharge (GCD) analysis and electrochemical

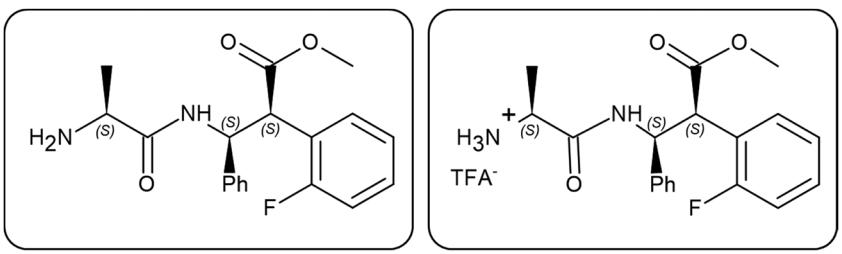

Scheme 1 Chemical structure of β-Fpg and the α/β-dipeptides studied in this work.

impedance spectroscopy (EIS). Results indicate that electrochemical symmetric SCs prepared using 3-layered electrodes made of **TFA·DP1** peptide assemblies located between two nano-structured PEDOT layers behave excellently and are very promising for use in wearable and implantable bioelectronic devices.

Methods

Peptide characterization

This work focusses on an α/β-dipeptide, which is based on the L-Ala-β-Fpg sequence with a specific stereochemistry of the $\beta^{2,3}$-diaryl-amino acid. The protected dipeptide was prepared according to a known procedure[35] from L-Ala and *syn*-3-amino-2-(2-fluorophenyl)-3-phenylpropanoic acid.

The procedure used for the *N*-terminal deprotection of the dipeptide is available in the literature as well as the characterization data for the free dipeptide (**DP1**).[36] The protonated form, **TFA·DP1**, was obtained directly by evaporating the reaction mixture without performing any extraction steps.

Since **TFA·DP1** characterization is not present in the literature, the NMR and MS (ESI) data are reported below, as well as the spectra in the SI.

TFA·DP1: ^{1}H NMR (300 MHz, CD_3OD): δ 7.66–7.60 (m, 1H), 7.50–7.44 (m, 2H), 7.42–7.28 (m, 4H), 7.25–7.18 (m, 1H), 7.18–7.10 (m, 1H), 5.71 (d, J = 11.7, 1H), 4.67 (d, J = 11.7, 1H), 3.68–3.58 (m, 1H), 3.44 (s, 3H), 1.22 (d, J = 6.76, 3H).

^{13}C NMR (75 MHz, $CDCl_3$): δ = 15.8, 48.3 (d, J = 2.4), 48.4, 51.2, 54.5, 115.1 (d, J = 23.3), 122.5 (d, J = 14.2), 124.3 (d, J = 3.6), 127.2, 127.8, 128.3, 129.2 (d, J = 3.1), 129.5 (d, J = 8.5), 139.8, 161.1 (d, J = 245.3), 171.0, 172.1.

^{19}F NMR (282 MHz, $CDCl_3$): δ = 77.0 (s, 3F, CF_3COO^-), −119.3 to −119.4 (m, 1F, *F*Ph).

MS (ESI): *m*/*z* calcd for $[C_{19}H_{21}FN_2O_3]$: 344.15; found: *m*/*z* 345.8 $[M+H]^+$.

PEDOT polymerization

Steel sheets (1.0 × 2.0 cm^2) were sanded and washed with Milli-Q® water, ethanol and acetone in an ultrasonic bath. Cleaned steel samples were covered with Kapton® tape leaving a central 0.5 × 0.5 cm^2 window (Scheme 2). The steel sheet was immersed in a three-electrode electrochemical cell with 10 mL of acetonitrile solution containing 50 μM of 3,4-ethylenedioxythiophene (EDOT) monomer and 0.1 M of $LiClO_4$ as a supporting electrolyte. The electrochemical setup was completed with the counter and the reference electrodes, which were a stainless-steel sheet of 10.0 × 1.0 cm^2 and Ag|AgCl in 3 M KCl, respectively. Then, a constant potential of 1.2 V was applied for 60 s to stabilize the system and, subsequently, potential sweeps between −0.5 V and +1.4 V were conducted at a scan rate of 50 mV s^{-1} for 3 min or 15 s. The resulting films were denoted PEDOT(3m) and PEDOT(15s), respectively.

Once the peptide was self-assembled on the PEDOT(3m) and PEDOT(15s) films generated using the procedure described above, the system was coated with a second PEDOT layer that was electrogenerated using as an electrolytic medium of 0.1 M $LiClO_4$ aqueous solution in which 50 μM of EDOT monomer was dissolved. The electrochemical setup was identical to that described above but the operational parameters were adapted to the new polymerization medium. More specifically, a potential of 1.0 V was applied for 60 s to stabilize the system and, subsequently, potential sweeps between −0.5 V and +1.0 V were conducted at a scan rate of 50 mV s^{-1} for 3 min or 15 s (*i.e.* in all cases, the t_p used for the layer prepared in aqueous solution was identical to the one used for the layer obtained in acetonitrile). All electrochemical polymerizations were performed at room temperature.

Peptide colloidal suspension

Peptide colloidal suspension (100 μL) was prepared from 100 mg mL^{-1} stocks using hexafluoroisopropanol (HFIP) as a solvent. The peptide concentration was adjusted by adding Milli-Q water (H_2O), ethanol (EtOH) or more HFIP, as a co-solvent in the necessary volumes. This choice was based on the utilization of biocompatible solvents, which is an intrinsic property of both PEDOT and peptides, as has been extensively reported in the literature. More specifically, peptide concentrations of 8, 4, 2 and 0.5 mg mL^{-1} were studied using HFIP : H_2O and HFIP : EtOH mixtures with 98 : 2, 20 : 80, 40 : 60, 60 : 40 and 80 : 20 ratios (in%). These ratios were chosen to prospect the whole range of mixtures, while the solubility of the peptides is preserved. Finally, 100 μL aliquots were placed on PEDOT substrates and stored at room temperature until dryness. The dielectric constant and the boiling point (ε and T_b, respectively) of the used solvents are ε = 16.7 and T_b = 59 °C for HFIP, ε = 24.3 and T_b = 78.2 °C for EtOH, and ε = 78.5 and T_b = 100 °C for H_2O. Accordingly, the polarity of HFIP:H_2O and HFIP:EtOH mixtures increased with the content of H_2O and EtOH, respectively, while their volatility decreased.

Characterization

Optical microscopy. Morphological observations were performed using a Zeiss Axioskop 40 microscope. Micrographs were taken with a Zeiss AxiosCam MRC5 digital camera.

Scanning electron microscopy (SEM). SEM studies were performed using a Focussed Ion Beam Zeiss Neon 40 scanning electron microscope operating at 5 kV and equipped with an EDX spectroscopy system. Samples were mounted on a double-sided adhesive carbon disc and sputter-coated with a thin layer of carbon to prevent sample charging problems.

Profilometry. Film thickness and roughness measurements were carried out using a Dektak 150 stylus profilometer (Veeco, Plainview, NY). Imaging of the films was conducted using the following optimized settings: tip radius = 2.5 μm; stylus force = 3.0 mg; scan length = 1 μm; and duration 30 seconds.

Atomic force microscopy (AFM). AFM images were obtained with a Molecular Imaging PicoSPM using a NanoScope IV controller under ambient conditions. The tapping mode AFM was operated at constant deflection. The row scanning frequency was set to 1 Hz. AFM measurements were performed on various parts of the films, which provided reproducible images. The statistical application of the NanoScope Analysis

software was used to determine the root mean square roughness (R_q), which is the average height deviation taken from the mean data plane.

X-ray photoelectron spectroscopy (XPS). XPS analyses were performed using a SPECS system equipped with a high-intensity twin-anode X-ray source XR50 of Mg/Al (1253 eV/1487 eV) operating at 150 W, placed perpendicular to the analyzer axis, and using a Phoibos 150 MCD-9 XP detector. The X-ray spot size was 650 mm. The pass energy was set to 25 and 0.1 eV for the survey and the narrow scans, respectively. Charge compensation was achieved with a combination of electron and argon ion flood guns. The energy and emission currents of the electrons were 4 eV and 0.35 mA, respectively. For the argon gun, the energy and the emission currents were 0 eV and 0.1 mA, respectively. The spectra were recorded with a pass energy of 25 eV in 0.1 eV steps at a pressure below 6×10^{-9} mbar. These standard conditions of charge compensation resulted in a negative but perfectly uniform static charge. The C1s peak was used as an internal reference with a binding energy of 284.8 eV. High-resolution XPS spectra were acquired by Gaussian/Lorentzian curve fitting after S-shape background subtraction. The surface composition was determined using the manufacturer's sensitivity factors.

Cyclic voltammetry (CV). CV assays were performed with an Autolab potentiostat–galvanostat, which was controlled with the Nova software. A standard three electrode cell was used to evaluate the current–potential response of the studied samples. Uncoated PEDOT(3m) and PEDOT(15s) films (control), peptide-coated PEDOT(3m) and PEDOT(15s) films (PEDOT(#) + **DP1** and PEDOT(#) + **TFA·DP1**, where # refers to 3m or 15s) films, and three-layered 2PEDOT(#)-**DP1** and 2PEDOT(#)-**TFA·DP1** electrodes, where # refers again to 3m or 15s were used as working electrodes (WEs). The counter electrode (CE) consisted of a stainless steel sheet (1.0×1.0 cm^2), while the reference electrode (RE) was an Ag|AgCl (KCl, 3 M) electrode. The electrochemical cell was filled with 10 mL of acetonitrile solution containing 0.1 M $LiClO_4$, which was used as electrolytic medium. The initial and final potentials were −0.90 V, while the reverse potential was +0.90 V. The scan rate was 50 mV s^{-1}.

Electrochemical characterization of symmetrical supercapacitors

Symmetrical SCs, which have been prepared as described in the next section, were characterized by CV, galvanostatic charge–discharge (GCD) analysis and electrochemical impedance spectroscopy (EIS). At least three independent replicas were performed for all experiments ($n \geq 3$).

Cyclic voltammetry. CV assays were performed with the equipment described in the previous sub-section using a standard three electrode cell. The electrolytic medium (10 mL) was an acetonitrile solution containing 0.1 M $LiClO_4$. The initial and final potential were 0.0 V, while the reverse potential was +0.90 V. Voltammograms were recorded at different scan rates, which ranged from 10 to 200 mV s^{-1}. The electrochemical stability was evaluated considering 200 consecutive redox cycles at a scan rate of 100 mV s^{-1}. All assays were performed at room temperature.

The loss of electrochemical activity (LEA, in %) against the increasing number of voltammetric cycles was expressed as:

$$\mathrm{LEA} = \frac{\Delta Q}{Q_{\mathrm{II}}} \times 100 \quad (1)$$

where ΔQ is the difference in voltammetric charges (in C) between the last and the second cycle, and Q_{II} is the voltammetric charge corresponding to the second cycle. Thus, a negative LEA value indicates a loss of electroactivity, while a positive LEA value refers to a gain of electroactivity.

The specific capacitance (sc; in F cm^{-2}) of the conducting polymer in the electrodes was calculated as:

$$\mathrm{sc} = \frac{Q}{\Delta V \cdot A} \quad (2)$$

where Q is the voltammetric charge, which is determined by integrating either the oxidative or the reductive part of the cyclic voltammetric curve, ΔV is the potential window, and A is the area of the electrode coated with polymer.

Galvanostatic charge–discharge assays. GCD assays were performed using the setup described for the CV analyses. Currents were chosen considering the CV results obtained at different scan rates. More specifically, the applied currents, which varied from 0.05 to 2.8 A, corresponded to the maximum current obtained for each sample at different scan rates. The stability test was conducted using the maximum current obtained by CV at 100 mV s^{-1}. The coulombic efficiency (η, %) of the SCs was evaluated as the ratio between the discharging and charging times (t_d and t_c, respectively) for the electrochemical window between 0.0 V and 0.8 V:

$$\eta = \left(\frac{t_d}{t_c}\right) \times 100 \quad (3)$$

Electrochemical impedance spectroscopy. EIS assays were performed using the setup previously described. Measurements were carried out by applying a sinusoidal voltage with an amplitude of 10 mV over a frequency range from 1 MHz to 0.1 Hz. The resulting data were processed and fitted to an electrical equivalent circuit (EEC) using Nova software. To ensure reproducibility, each sample was tested in triplicate.

Results and discussion

Preparation and characterization of the PEDOT substrate

Fig. 1 shows representative SEM micrographs of the morphologies found at the surface of PEDOT films electrodeposited using acetonitrile as a solvent and t_p = 3 min and 15 s, hereafter denoted PEDOT(3m) and PEDOT(15s). These values of t_p were selected to obtain films with very different surface morphologies and thicknesses. PEDOT(3m) displayed a globular morphology formed by the aggregation of micrometric globules (Fig. 1a), thus evidencing a three-dimensional (3D) growth. Conversely, PEDOT(15s) films showed a significantly flatter

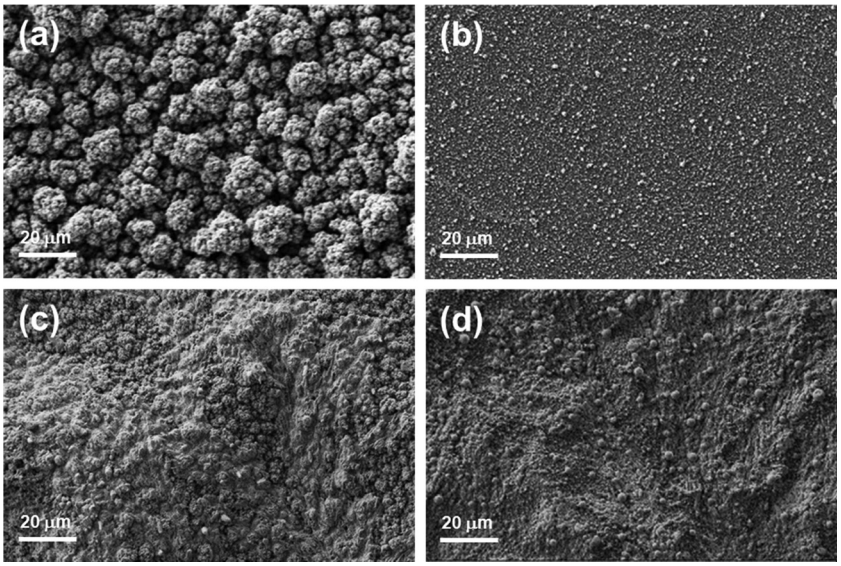

Fig. 1 Representative SEM images of PEDOT films prepared in (a and b) acetonitrile and (c and d) water using a t_p of (a and c) 3 min and (b and d) 15 s.

morphology with a dense packing of nanometric particles, which was closer to two-dimensional (2D) growth (Fig. 1b). These results indicated the formation of multiple nucleation centers during the first steps of the electropolymerization process, giving rise to a relatively flat film. After that, there was preferential growth over some nucleation centers, probably due to steric effects, resulting in the formation of nanometric particles first (t_p = 15 s) and micrometric globules later (t_p = 3 min). The morphological differences between PEDOT(3m) and PEDOT(15s) were expected to play a key role in peptide self-assembly, since these substrates act as templates during this process.

Other crucial parameters for understanding both the peptide self-assembly and the electrode performance are the thicknesses (L) and the R_q of the films. These were determined using profilometry (for all films) and AFM scratching technology (for PEDOT(15s) films, since the roughness was too high for PEDOT(3m)), the latter having a higher level of accuracy due to its precise tip and lower loading force (Fig. S1). In addition to the good agreement between profilometry and AFM scratching, results (Table 1) confirmed that both L and R_q were much higher for PEDOT(3m) than for PEDOT(15s).

Although they were not used as templates in the self-assembly of the peptides, to better understand the functioning of the 3-layered electrodes, L and R_q were also determined for the PEDOT(3m) and PEDOT(15s) films electrogenerated in water. The values of L and R_q obtained for films produced using the same t_p were significantly lower in water than in acetonitrile. These observations indicated that the polymerization rate relative to deposition charge density of PEDOT synthesized in acetonitrile was 2.5 (t_p = 3 min) and 4.5 (t_p = 15 s) times higher than that achieved in aqueous solution. These observations were fully consistent with data reported in the literature.[38] On the other hand, SEM images showed that the cauliflower structure of PEDOT aggregates in PEDOT(3m) films was much less pronounced in water (Fig. 1c), while the morphology of PEDOT(15s) was less homogeneous in water (Fig. 1d) than in acetonitrile. These differences were attributed to the different solubility of EDOT oligomers produced during the initial stages of electropolymerization in these solvents.[39]

Optimizing the assembly of DP1 on PEDOT

The self-assembly of **DP1** was examined using a bottom-up approach in which the concentrations and solvents listed in Table S1 were considered (labeled as conditions A–T). Initially, all experiments were conducted using PEDOT(3m) substrates. Assays with a dilute peptide concentration (0.5 mg mL^{-1}) using HFIP : H_2O and HFIP : EtOH mixtures (conditions A–D in Table S1) evidenced that **DP1** aggregation was favored when the polarity and volatility of the medium decreased and increased,

Table 1 Thickness (L) and root mean square roughness (R_q) of PEDOT(3m) and PEDOT(15s) produced in acetonitrile and water, as determined by profilometry and AFM scratching

		PEDOT(3m)		PEDOT(15s)	
Solvent	Technique	L	R_q	L	R_q
Acetonitrile	Profilometry	8.4 ± 2.4 μm	4.7 ± 1.6 μm	1.4 ± 0.3 μm	251 ± 41 nm
	AFM	—	—	1.1 ± 0.4 μm	299 ± 72 nm
Water	Profilometry	3.4 ± 1.0 μm	1.4 ± 0.4 μm	0.6 ± 0.1 μm	300 ± 51 nm
	AFM	—	—	0.4 ± 0.1 μm	228 ± 59 nm

respectively (*i.e.* when the content of HFIP in the mixtures increased from 2% to 20%). Despite these changes, the amount of peptide was not high enough to promote the formation of fibrillary or regularly shaped structures, as shown in Fig. S2.

Optical micrographs recorded for assemblies derived from 2 mg mL^{-1} peptide solutions (conditions E–N in Table S1), which are displayed in Fig. S3, confirmed the importance of the peptide concentration, as well as of the polarity and volatility of the medium. When the polarity and volatility of the medium were low and high, respectively, unshaped peptide aggregates were obtained (conditions E–H), while when there was a balance between polarity and volatility with 60 : 40 and 40 : 60 ratios (conditions I–K), well-shaped microfibers were formed. Finally, when the volatility was very high (conditions L–N), the peptide acted as a coating covering the whole PEDOT surface.

In order to favor the formation of more abundant and bigger fibers, the concentration of **DP1** was increased to 4 mg mL^{-1}, while the solvent : co-solvent ratios were maintained at 40 : 60 and 60 : 40 (conditions O–R in Table S1). Results displayed in Fig. S4 show that the peptide preserved well-defined and shaped fibers only for HFIP:H_2O mixtures, while unstructured heterogeneous aggregates that partially coated the PEDOT surface were derived from HFIP:EtOH mixtures. Thus, the polarity and volatility of HFIP:EtOH, which were lower and higher, respectively, than those of HFIP:H_2O for the same ratio, did not allow the formation of fibers when peptide molecules are in excess. Instead, increasing the peptide concentration had a positive effect on the self-assembly to form fibers when the medium is 60 : 40 and 40 : 60 HFIP : H_2O.

Three-layered DP1-containing electrode manufacturing

At this stage, 8 mg mL^{-1} **DP1** solution in 40 : 60 HFIP : H_2O (condition S) was selected to construct three-layered electrodes, which were prepared using both PEDOT(3m) and PEDOT(15s) films. Fig. 2a and b display representative SEM micrographs of the fibers formed on two such substrates by dropping 100 μL of the prepared **DP1** solution. The thickness of the formed fibers was much higher for the roughest surface (*i.e.* fibers up to 10 μm thick were observed on PEDOT(3m), while the average thickness of the fibers obtained on PEDOT(15s) was 1–2 μm). Interestingly, Shezad *et al.*[40] reported that a rough surface decelerates the two-dimensional diffusion of peptides on the surface, which causes a retardation of the kinetic pathway for the formation of new nuclei and fibers. However, this only

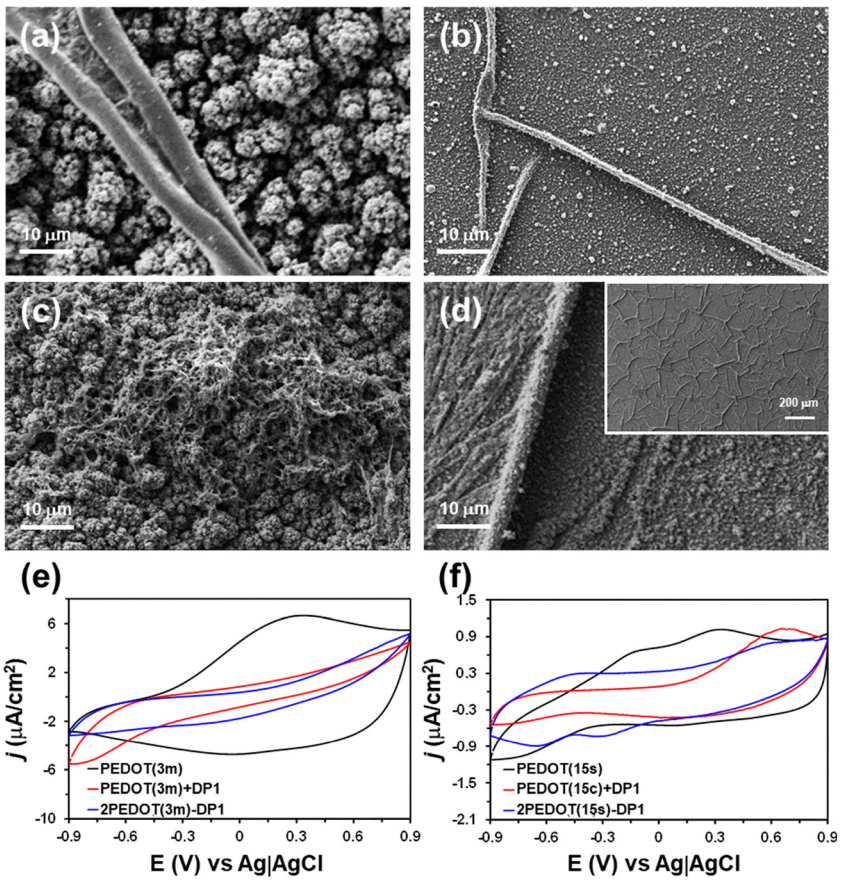

Fig. 2 Representative SEM micrographs of **DP1** fibers formed on the surface of (a) PEDOT(3m) and (b) PEDOT(15s) films by dropping 100 μL of a 8 mg mL^{-1} **DP1** solution in 40 : 60 HFIP : H_2O. (c and d) Representative SEM micrographs of (c) 2PEDOT(3m)-**DP1** and (d) 2PEDOT(15s)-**DP1** three-layered electrodes. Cyclic voltammograms recorded for pristine PEDOT films, PEDOT films with **DP1** fibers on the surface (PEDOT + **DP1**) and 2PEDOT-**DP1** electrodes, where PEDOT films were prepared using a t_p of (e) 3 min and (f) 15 s.

applied when extremely flat polymeric surfaces were compared (*i.e.* R_q of the polymeric substrates studied by Shezad *et al.*[40] ranged between 0.26 and 1.81 nm). The R_q of the two PEDOT surfaces examined in this work (Table 1) was incommensurately large relative to those examined by Shezad *et al.*,[40] suggesting that such observation is not valid at the micrometric scale. Indeed, results displayed in Fig. 2a and b suggest that the inter-peptide association is more favored for the PEDOT(3m) substrate than for the PEDOT(15s) one. Thus, in the former PEDOT substrate the enthalpic contribution dominated and accelerated the aggregation process, whereas in the latter one the entropic contribution competed with the enthalpic one.

It is well-known that multilayered electrodes made layer-by-layer by alternating compounds with markedly different electrochemical properties exhibit better performance than monolayered electrodes prepared using the same amount of a single electroactive material.[18,41,42] This behavior, which was mainly studied using PEDOT layers separated by a less conductive intermediate layer (*e.g.* a less conductive polymer, like poly(*N*-methyl-pyrrole) and exfoliated clays), was attributed to the dielectric breakage induced by the latter. Inspired by such studies, another PEDOT layer was electrodeposited on the surface of the PEDOT film coated with **DP1** fibers (Scheme 2). This second layer of PEDOT was electropolymerized using a $LiCO_4$ aqueous solution as the electrolytic medium instead of a $LiClO_4$ acetonitrile solution (see Methods section), which avoided dissolving the **DP1** fibers in an organic solvent.

Fig. 2c and d displays SEM micrographs of the two resulting three-layered electrodes: (1) PEDOT(3m) electropolymerized using $LiClO_4$ dissolved in acetonitrile + **DP1** fibers + PEDOT(3m) electropolymerized using $LiClO_4$ dissolved in water, hereafter named 2PEDOT(3m)-**DP1**; and (2) PEDOT(15s) electropolymerized using $LiClO_4$ dissolved in acetonitrile + **DP1** fibers + PEDOT(15s) electropolymerized using $LiClO_4$ dissolved in water, hereafter named 2PEDOT(15s)-**DP1**. As can be seen, in both cases **DP1** fibers were completely coated by the second PEDOT layer. However, a significant difference was found between the two electrodes. While the thickness of the second PEDOT layer was large enough to hide the intermediate **DP1** fibers in 2PEDOT(3m)-**DP1** (Fig. 2c), the shape of the **DP1** fibers can be clearly recognized below the second layer of PEDOT in 2PEDOT(15s)-**DP1** (Fig. 2d). Thus, the thin thickness of the second layer allowed the fibers to act as a template in the second electrode.

The thickness of 2PEDOT(3m)-**DP1** and 2PEDOT(15s)-**DP1** electrodes was 14.3 ± 3.1 μm and 4.9 ± 0.5 μm, as determined by profilometry. It is worth noting that these values were higher than those obtained as the sum of individual films polymerized in acetonitrile and in water (according to Table 1: 11.8 ± 3.4 and 2.0 ± 0.4 μm for t_p = 3 min and 15 s, respectively). This effect was much more pronounced for 2PEDOT(15s)-**DP1** in which the thickness of the film was more than twice the thickness of two individual films. It should be noted that, although this increase can initially be associated with the peptide fibers in the intermediate layer, the increase in thickness must be mainly attributed to the synergistic effect of the first PEDOT layer on the polymerization of the second layer. In order to demonstrate this, bilayer PEDOT systems were prepared, eliminating the intermediate peptide layer. The thickness of the resulting systems, called 2PEDOT(3m) and 2PEDOT(15s), was similar to those of 2PEDOT(3m) + **DP1** and 2PEDOT(15s) + **DP1** (*i.e.* the difference in the thickness of the bilayer and trilayer systems was smaller than 10%).

Finally, the electrochemical characterization was performed by CV using a potential range from −0.9 V to +0.9 V. Fig. 2e and f compares representative cyclic voltammograms recorded for: (1) PEDOT(3m) and PEDOT(15s) films without peptide; (2) the same films coated with peptide fibers, hereafter denoted PEDOT(3m) + **DP1** and PEDOT(15s) + **DP1**, respectively; and (3) the three-layered electrodes, 2PEDOT(3m)-**DP1** and 2PEDOT(15s)-**DP1**. As was expected, the electrochemical response increased with the amount of conducing polymer, being much higher for systems prepared using t_p = 3 min than for systems obtained using t_p = 15 s. Furthermore, the electrochemical activity, which is related to the voltammetric charge and, therefore, to the area of the voltammogram, is much higher for uncoated PEDOT films than for peptide-coated PEDOT + **DP1** films, regardless of t_p. This feature indicates that, as expected, the electrical response of the peptide is lower than that of PEDOT, suggesting that **DP1** fibers can effectively induce a dielectric breakage between layers and improve the properties of PEDOT-based multilayered electrodes.

On the other hand, 2PEDOT(3m)-**DP1** and 2PEDOT(15s)-**DP1** electrodes displayed different behaviors. While the electroactivity of 2PEDOT(3m)-**DP1** was even smaller than that of PEDOT(3m) + **DP1**, the electrochemical activity was greater for 2PEDOT(15s)-**DP1** than for PEDOT(15s) + **DP1**. These results, together with the thickness of deposited fibers (*i.e.* up to 10 μm thick) and the R_q of PEDOT(3m) (Table 1), suggest that, probably, the second PEDOT(3m) layer is not in contact with the first one, which could explain the reduction in the electroactivity. Instead, the increase in electroactivity of 2PEDOT(15s)-**DP1** with respect to PEDOT(15s) + **DP1** suggests a good coupling between successive layers. However, the favorable inter-connection between the two thin conducting polymer layers is locally interrupted by **DP1** peptide fibers distributed in the intermediate layer. Although aromatic-rich **DP1** fibers exhibit electrochemical response, the electrical response of the peptide fibers is clearly lower than that of PEDOT layers and, therefore, the electrical behaviors of **DP1**/**DP1** and PEDOT/**DP1** interfaces in 2PEDOT(15s)-**DP1** are expected to be very different. By similarity with previously reported multilayered electrodes, these interfaces have been inferred as series and parallel connections, respectively, while the peptide fibers forming the intermediate layer are considered as micro-dielectrics with respect to PEDOT layers. Accordingly, these micro-dielectric elements are interconnected in series while they form parallel interconnections with PEDOT(15s) layers. Nevertheless, from a practical point of view, the electrochemical activities of 2PEDOT(3m)-**DP1** and 2PEDOT(15s)-**DP1** electrodes were lower than those of PEDOT(3m) and PEDOT(15s). Therefore, the **DP1** peptide was discarded for the preparation of electrodes for energy storage applications.

Optimizing the self-assembly of TFA·DP1 on PEDOT

The strategy used to explore the self-assembly of **TFA·DP1** on PEDOT(3m) was similar to that described above for **DP1**. In this case, the peptide concentrations and solvent mixtures (conditions a–k in Table S2) were selected considering both the results obtained for **DP1** and the solubility of **TFA·DP1**. When the **TFA·DP1** concentration was as low as 0.5 mg mL^{-1} and the HFIP : H_2O ratio was varied from 2 : 98 to 80 : 20 (conditions a–c in Table S2), poorly defined fibrillary structures could be observed when the volatility of the solvent:co-solvent mixture was the highest (Fig. S5). No significant improvement was observed when the peptide concentration was increased to 2 mg mL^{-1}, or even when the volatility of the medium was enhanced by replacing water by EtOH (Fig. S6; conditions d–i in Table S2). After several tests and increasing the peptide concentration to 4 mg mL^{-1}, we noted that the only condition that produced a slight nanostructuring of **TFA·DP1** was when a medium with intermediate polarity and volatility, 98 : 2 EtOH : HFIP (condition j in Table 2), was used. This is reflected in Fig. 3a, which shows representative SEM micrographs of the peptide coating. As is shown, **TFA·DP1** organizes in ultrathin nanofibrillary structures that form a continuous network without altering the intrinsic porosity of the PEDOT(3m) substrate.

Three-layered TFA·DP1-containing electrode manufacturing

At this stage, an 8 mg mL^{-1} **TFA·DP1** solution in 2 : 98 HFIP : EtOH was selected to manufacture both PEDOT(3m)- and PEDOT(15s)-based three-layered electrodes. However, the increase of the peptide concentration from 4 to 8 mg mL^{-1} produced some changes in the assembly of the unprotected peptide with respect to that displayed in Fig. 3a, especially when the PEDOT substrate was the roughest. Fig. 3b and c shows the assemblies obtained for the peptide deposited on PEDOT(3m) and PEDOT(15s), respectively. While **TFA·DP1** formed globular aggregates of variable size on PEDOT(3m) (Fig. 3b), long fibrillary structures of micrometric thickness were regularly observed on PEDOT(15m) (Fig. 3c). These results support the aforementioned hypothesis, indicating that, when the peptide concentration is very high, the roughest substrate, PEDOT(3m), prioritizes an enthalpic contribution that, in this case, is dominated by strong non-specific electrostatic interactions, giving rise to disordered aggregates. In contrast, both the entropic and enthalpic contributions compete when the peptide is deposited on PEDOT(15s), facilitating the formation of ordered self-assembled structures.

SEM images of the electrodes derived by adding the layer electrogenerated in water, hereafter denoted 2PEDOT(3m)-**TFA·DP1** and 2PEDOT(15s)-**TFA·DP1**, are shown in Fig. 3d and e. As occurred for **DP1**-based electrodes, the **TFA·DP1** was completely coated and hidden by the second layer of conducting polymer in 2PEDOT(3m)-**TFA·DP1** (Fig. 3d), whereas the shape of the coated peptide fibers is easily identified in 2PEDOT(15s)-**TFA·DP1** (Fig. 3e). However, since **TFA·DP1** is water-soluble, there is a possibility that the peptide acted as a template that dissolved in the electrolytic medium during the incorporation of the third layer. In order to confirm that **TFA·DP1** remained in the intermediate layer of the electrode after electropolymerizing the last PEDOT layer using an aqueous electrolytic medium, XPS studies were performed for both 2PEDOT(3m)-**TFA·DP1** and 2PEDOT(15s)-**TFA·DP1** electrodes. The XPS survey spectra, which are displayed in Fig. 4a and b, indicated that the two electrodes contain fluorine, oxygen, nitrogen, carbon and sulfur intensities at approximately 687, 532, 401, 285 and 167 eV, respectively.

The atomic percent compositions of 2PEDOT(3m) (control), 2PEDOT(3m)-**TFA·DP1** and 2PEDOT(15s)-**TFA·DP1** are compared in Table 2. The composition of the control was consistent with that expected for perchlorate-doped PEDOT, with a small fraction of nitrogen contaminating the sample. However, the S 2p : N 1s ratio, which was approximately 35 for 2PEDOT(3m), decreased to 0.36 and 0.46 for 2PEDOT(3m)-**TFA·DP1** and 2PEDOT(15s)-**TFA·DP1**, respectively, evidencing a source of nitrogen different from the impurities found in the 2PEDOT(3m) electrode (Fig. S7). The high resolution N 1s spectra of 2PEDOT(3m)-**TFA·DP1** and 2PEDOT(15s)-**TFA·DP1** electrodes showed two peaks centered at around 402 and 400 eV, which were associated with the N–H and N–C bonds of the peptide group, respectively (Fig. 4c and d). The presence of **TFA·DP1** at the electrode was also confirmed by the content of fluorine (Table 2), which was not detected for the control. The high resolution spectra of F 1s reflected a single peak at around 687 eV, which was assigned to the F–C bonds from both the TFA stabilizing ions and the β-2*S*,3*S*-Fpg residue (Fig. S8).

Fig. 4e and f compare the cyclic voltammograms recorded for the 3-layered 2PEDOT(3m)/**TFA·DP1** and 2PEDOT(15s)/**TFA·DP1** electrodes with those obtained for uncoated and peptide-coated conducting polymer films (*i.e.* PEDOT(3m), PEDOT(15s), PEDOT(3m) + **TFA·DP1** and PEDOT(15s) + **TFA·DP1**). As can be seen, the electrochemical activities of 2PEDOT(3m)-**TFA·DP1**, PEDOT(3m) + **TFA·DP1** and PEDOT(3m) were very similar, suggesting that any peptide-induced effect was practically negated by the excessive thickness and roughness of the PEDOT layers (Table 1). Conversely, the area of the voltammogram recorded for 2PEDOT(15s)-**TFA·DP1** was 41% and 38% times greater than those of PEDOT(15s)-**TFA·DP1** and PEDOT(15s), respectively, evidencing that the dielectric breakage induced by the intermediate peptide fibers is manifested when PEDOT layers are thin and flat enough (*i.e.* thickness $\leq$ 1.5 Å and $R_q \leq$ 300 nm). Thus, in PEDOT(15s)-**TFA·DP1**, self-assembled **TFA·DP1** structures behave as micro-dielectrics with respect to PEDOT(15s) layers, forming parallel interconnections. Furthermore, the improvement with respect to PEDOT(15s)-**DP1** has been attributed to the electrical response of TFA anions (*i.e.* ions flow), which is added to electronic response (*i.e.* electrons flow).

Table 2 Atomic percent composition (atomic%) of 2PEDOT(3m)-**TFA·DP1**, 2PEDOT(15s)-**TFA·DP1** and 2PEDOT(3m) electrodes

	C 1s	O 1s	S 2p	N 1s	F 1s
2PEDOT(3m)-**TFA·DP1**	54.50	42.32	0.71	1.94	0.53
2PEDOT(15s)-**TFA·DP1**	58.00	38.73	0.68	1.47	1.11
2PEDOT(3m)	60.24	35.82	3.83	0.11	—

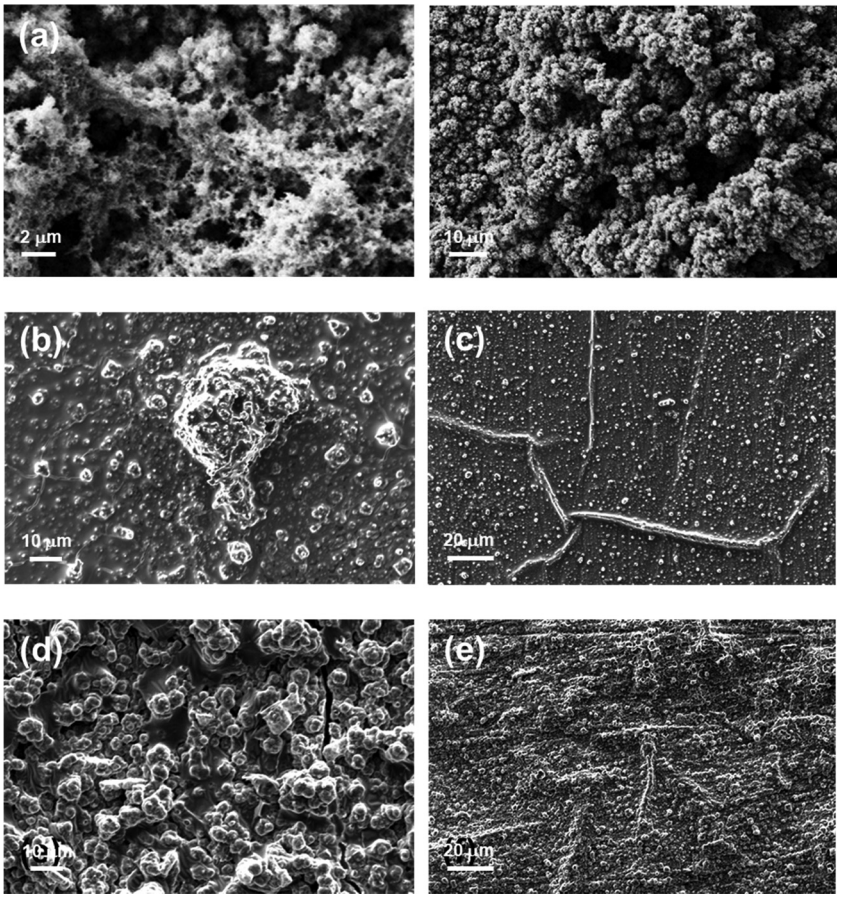

Fig. 3 (a) Representative SEM micrographs at high and low magnifications (left and right, respectively) of the nanostructured **TFA·DP1** assemblies from a 4 mg mL^{-1} solution on PEDOT(3m) using condition j (Table S2). (b and c) Representative SEM micrographs of **TFA·DP1** globules and fibers formed on the surface of (b) PEDOT(3m) and (c) PEDOT(15s) films, respectively, from a 8 mg mL^{-1} peptide solution. (d and e) Representative SEM micrographs of (d) 2PEDOT(3m)-**TFA·DP1** and (e) 2PEDOT(15s)-**TFA·DP1** electrodes.

Although the peptide-induced improvement was much more evident for 2PEDOT(15s)-**TFA·DP1** than for 2PEDOT(3m)-**TFA·DP1**, both electrodes were considered for constructing symmetric SCs.

Electrochemical performance of 2PEDOT-TFA·DP1 electrodes in symmetrical capacitors

SCs can be constructed using three different configurations. Type 1 uses two identical electrodes made with a p-doped conducting polymer (symmetric SCs), while type 2 uses two different p-doped conducting polymers as electrodes (asymmetric SCs). Finally, electrodes in type 3 are made with the same conducting polymer but using the p-and n-doped forms as positive and negative electrodes, respectively. In this work, type 1 symmetric SCs were constructed using two identical electrodes of 3-layered 2PEDOT(3m)-**TFA·DP1** or 2PEDOT(15s)-**TFA·DP1**, and an acetonitrile solution containing 0.1 M $LiClO_4$, as an electrolytic medium, as indicated in Scheme 3.

The electrochemical behavior of SCs containing 2PEDOT(3m)-**TFA·DP1** and 2PEDOT(15s)-**TFA·DP1** electrodes was investigated by CV, GCD curves and EIS. Results were compared with those obtained for control electrochemical SC devices, which were prepared using two identical 2-layered PEDOT films as electrodes, 2PEDOT(3m) or 2PEDOT(15s); more specifically, electrodes prepared without incorporating the **TFA·DP1** peptide at the intermediate layer.

Cyclic voltammetry. Cyclic voltammograms for the symmetric SCs constructed using 2PEDOT(3m) and 2PEDOT(15s) electrodes (controls), which were recorded from 0.0 to 0.9 V at scan rates ranging from 10 to 200 mV s^{-1}, are shown in Fig. 5a and b (left). Due to the amount of electroactive material, the electrochemical activity, which increased with the scan rate, was higher for 2PEDOT(3m) than for 2PEDOT(15s) at each scan rate. Furthermore, Fig. 5a and b (right) demonstrate the linear correlation between the current at the reversal potential and the square root of the scan rate, suggesting a diffusion controlled process. On the other hand, cyclic voltammograms acquired at different scan rates for SCs prepared using peptide-containing electrodes (Fig. 5c and d) reflected an increment in the electrochemical activity with respect to the devices without peptide at the intermediate layer. For the SC prepared with the 2PEDOT(3m)-**TFA·DP1** electrode, the area of the voltammograms increased by 39% with respect to that of 2PEDOT(3m), while this increment was much greater (*i.e.* 358%) for 2PEDOT(15s)-**TFA·DP1** with respect to 2PEDOT(15s).

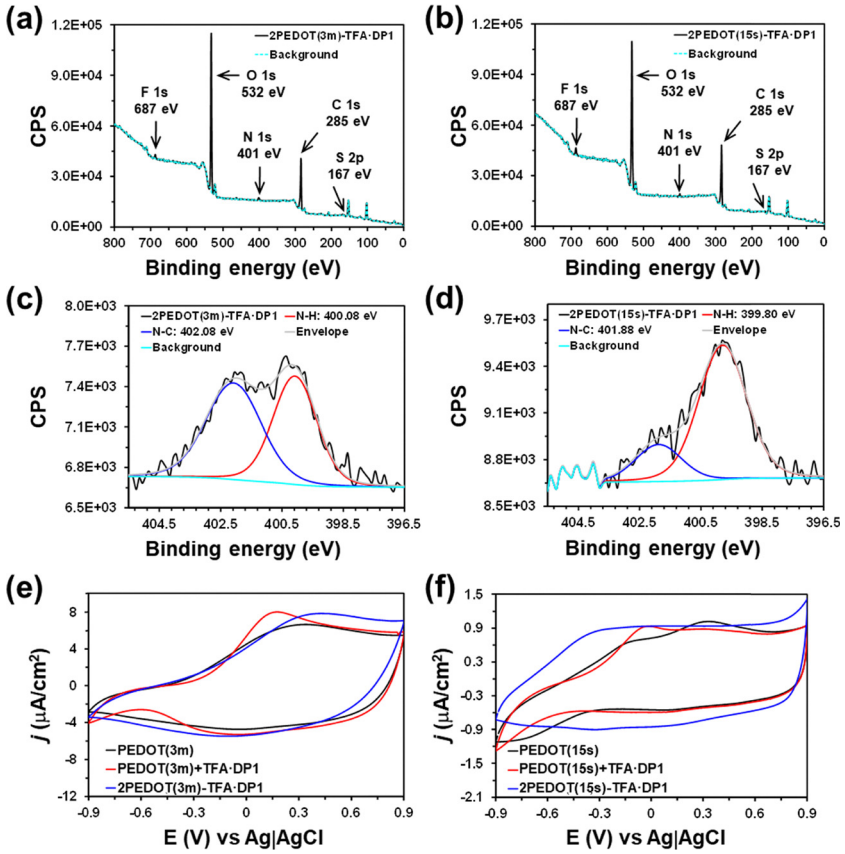

Fig. 4 (a and b) XPS survey spectrum and (c and d) high resolution N 1s spectrum of (a and c) 2PEDOT(3m)-**TFA·DP1** and (b and d) 2PEDOT(15s)-**TFA·DP1** electrodes. (e and f) Cyclic voltammograms recorded for pristine PEDOT films, PEDOT films coated with **TFA·DP1** fibers on the surface (PEDOT + **TFA·DP1**) and 2PEDOT-**TFA·DP1** electrodes, where PEDOT films were prepared using a t_p of (e) 3 min and (f) 15 s.

For 2PEDOT(3m)-**TFA·DP1**, the reversal peak currents are linearly proportional to the square root of the scan rate (Fig. 5c, right), indicating that the substrate redox process is limited by diffusion. The relative similarity between 2PEDOT(3m) and 2PEDOT(3m)-**TFA·DP1** indicated that the electrochemical processes were independent of peptide–conducting polymer interactions, as they were probably shielded by the external thick PEDOT(3m) layer. In the case of 2PEDOT(15s)-**TFA·DP1**, the reversal current is linearly proportional to the scan rate (Fig. 5d, right), which suggests that a surface confined process occurs. This is due to the physical adsorption of ions to the thin PEDOT(15s) layer *via* coulombic forces, which possibly occurs *via* the mediation of surface-confined, but still accessible, **TFA·DP1** peptide fibers.

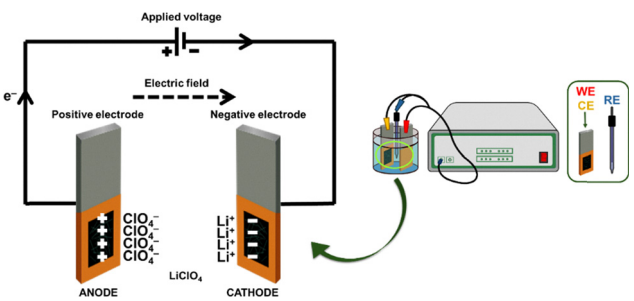

Scheme 3 Sketch of the symmetric SCs constructed using 2PEDOT(3m)-**TFA·DP1** or 2PEDOT(15s)-**TFA·DP1** electrodes.

The stability of the two **TFA·DP1**-containing devices was evaluated by considering 200 cycles of CV. Selected voltammograms recorded for SCs made of 2PEDOT(3m) and 2PEDOT(3m)-**TFA·DP1** are compared in Fig. 6a and b. The behavior of the two systems was completely different, as is also evidenced by the variation of the LEA (eqn (1)) with the number of CV cycles (Fig. 6c). For 2PEDOT(3m), the area of the voltammograms increased for the first 20 cycles (Fig. 6a), reflecting a self-stabilizing effect that increased the electroactivity by almost 20%. After that, the electroactivity decreased with increasing number of cycles, even though the LEA after 200 cycles remained positive (*i.e.* the voltammetric charge was higher after 200 cycles than after 2 cycles). This evidenced the high electrochemical stability of 2PEDOT(3m) electrodes. In contrast, the electroactivity of 2PEDOT(3m)-**TFA·DP1** decreased rapidly with increasing number of cycles (Fig. 6b). Indeed, the LEA, which exhibited negative values during the 200 cycles, evidenced a reduction in the electroactivity close to 75% (Fig. 6c). This was attributed to the poor contact between the PEDOT layers at the interface with the peptide, which becomes worse when the peptide degrades by applying consecutive oxidation–reduction cycles.

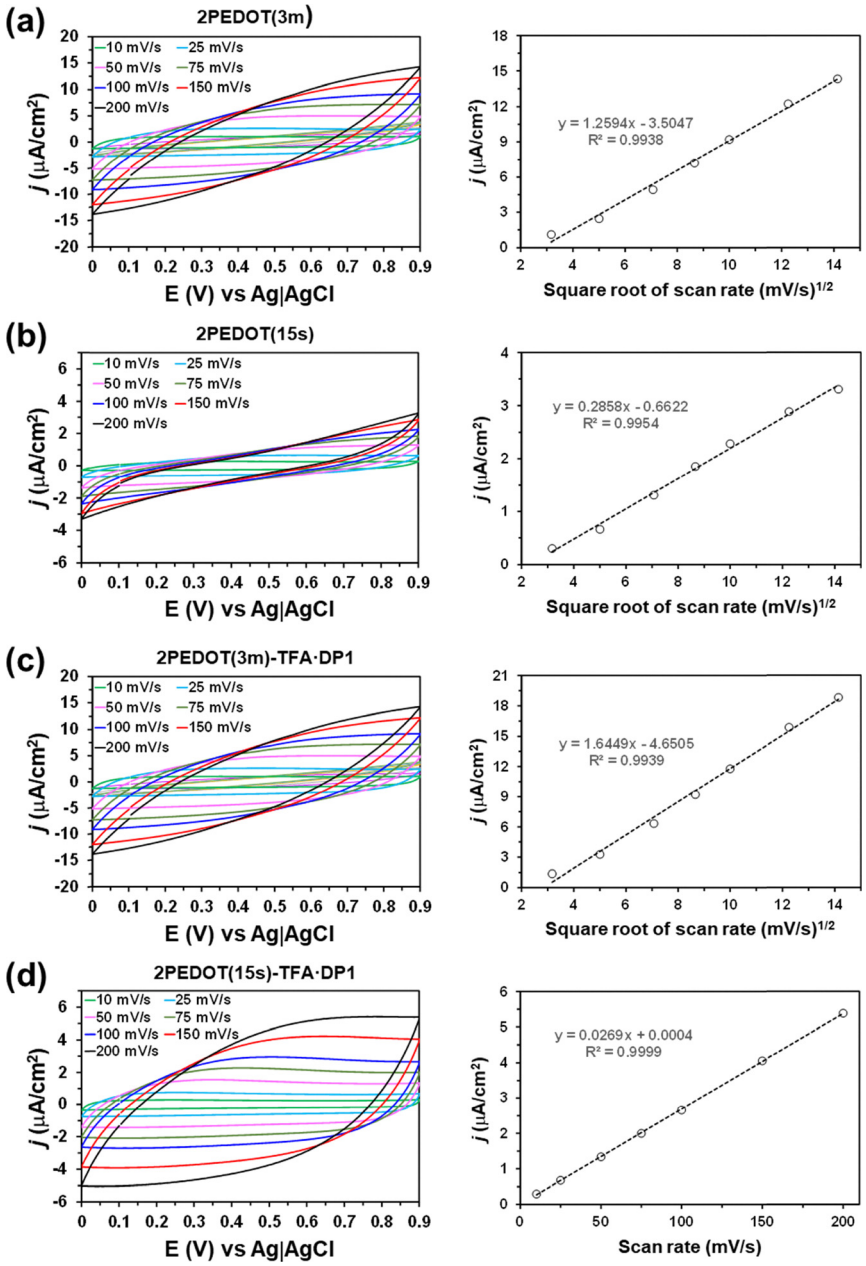

Fig. 5 Cyclic voltammograms at different scan rates (left) and current at the reversal potential *vs.* (a–c) the square root of the scan rates or (d) the scan rate (right) for symmetric SCs constructed with (a) 2PEDOT(3m), (b) 2PEDOT(15s), (c) 2PEDOT(3m)-**TFA·DP1** and (d) 2PEDOT(15s)-**TFA·DP1** electrodes.

Fig. 6d and e display the cyclic voltammograms recorded after 2, 5, 10, 25, 50, 75, 100, 150 and 200 consecutive redox cycles recorded for the 2PEDOT(15s) and 2PEDOT(15s)-**TFA·DP1** electrodes. As can be seen, the electrochemical stability of the two electrodes is extremely high. Specifically, the reduction in the electroactivity after 200 cycles with respect to the second cycle was as low as 2% and 5% for 2PEDOT(15s) and 2PEDOT(15s)-**TFA·DP1**, respectively (Fig. 6f), confirming that, in the latter electrode, the intermediate peptide layer works efficiently allowing the contact between the two outer PEDOT layers.

On the other hand, Fig. 7a compares the variation of the difference between electrochemical activities (ΔE_A) for electrodes prepared applying the same t_p with and without incorporating the intermediate peptide layer (*i.e.* 2PEDOT(3m)-**TFA·DP1** *vs.* 2PEDOT(3m) and 2PEDOT(15s)-**TFA·DP1** *vs.* 2PEDOT(15s)). As was previously observed (Fig. 5), the ΔE_A of 2PEDOT(3m) is twice that of 2PEDOT(3m)-**TFA·DP1** at the 2nd cycle (*i.e.* ΔE_A = ~50%). This difference became much more pronounced with increasing number of cycles, stabilizing at ~11% after 75 cycles. Conversely, the electroactivities of 2PEDOT(15s)-**TFA·DP1** and 2PEDOT(15s) were very similar, differing by less than 8%, regardless of the number of redox cycles. The specific capacitance (sc; eqn (2)) derived from the recorded voltammograms reflects this behavior (Fig. 7b). While

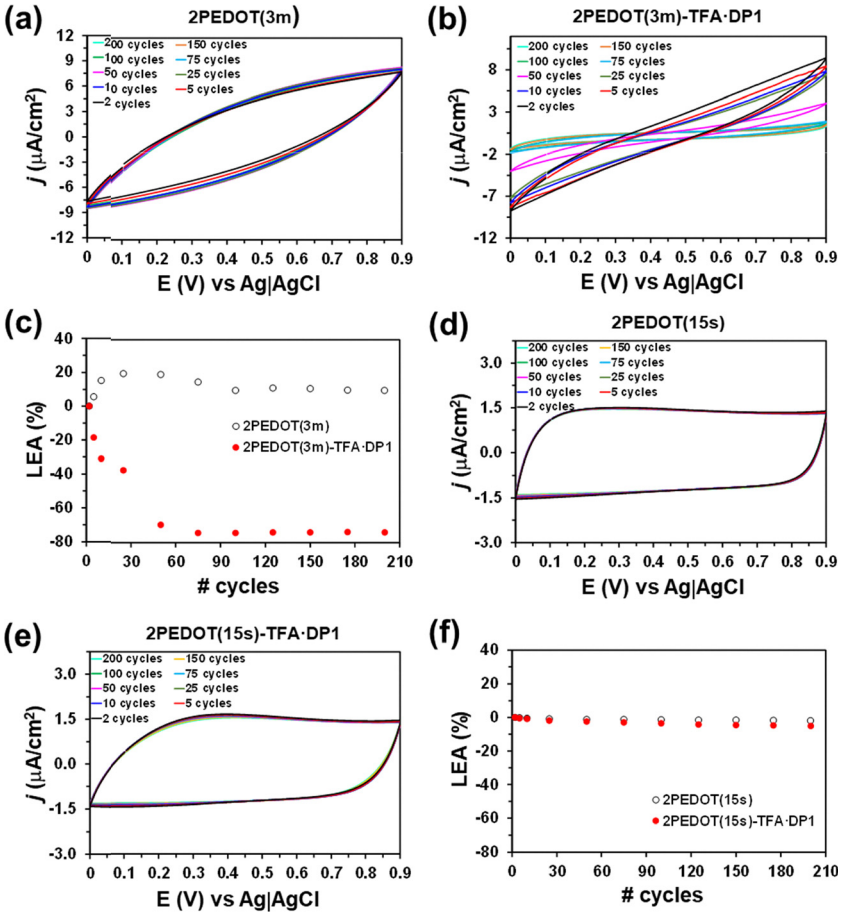

Fig. 6 (a–f) Electrochemical stability of the studied symmetrical SCs. Cyclic voltammograms recorded after 2, 5, 10, 25, 50, 75, 100, 150 and 200 consecutive redox cycles for (a) 2PEDOT(3m), (b) 2PEDOT(3m)-**TFA·DP1**, (d) 2PEDOT(15s) and (e) 2PEDOT(15s)-**TFA·DP1** electrodes. Variation of the loss of electroactivity (LEA; eqn (1)) with the number of redox cycles for (c) 2PEDOT(3m) and 2PEDOT(3m)-**TFA·DP1** and (f) 2PEDOT(15s) and 2PEDOT(15s)-**TFA·DP1**.

the specific capacitance is much higher for 2PEDOT(3m) than for 2PEDOT(3m)-**TFA·DP1** after 2 and 200 redox cycles (207.6 *vs.* 26.0 mF cm^{-2} and 228.3 *vs.* 6.8 mF cm^{-2}, respectively), the specific capacitances obtained for 2PEDOT(15s) and 2PEDOT(15s)-**TFA·DP1** are very similar and independent of the number of redox cycles (*i.e.* around 47 mF cm^{-2} in all cases).

Electrodes fabricated by combining conducting polymers with other intrinsically conducting materials (*e.g.* graphene, carbon nanotubes and metallic nanoparticles) often exhibit specific capacitances exceeding those obtained in this work for 2PEDOT(3m)-**TFA·DP1** and 2PEDOT(15)-**TFA·DP1**, in some cases by up one order of magnitude.[43] However, the specific capacitances measured for the α/β-dipeptide-based supercapacitors studied here are comparable to those reported for devices employing electrodes with similar constituents (*i.e.* PEDOT and peptides). For example, supercapacitors assembled with

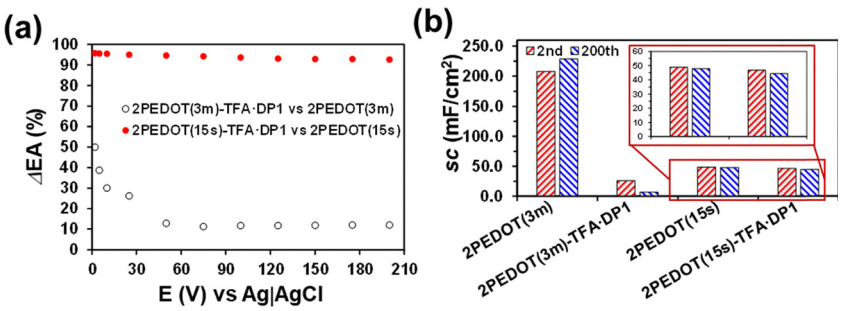

Fig. 7 (a) Effect of the **TFA·DP1** peptide on the electrochemical activity (ΔE_A) of 2PEDOT(3m) and 3PEDOT(15s) electrodes and its variation with the number of redox cycles. (b) Comparison of the specific capacitances (sc) determined for the studied electrodes after 2 and 200 redox cycles.

electrodes composed of a polypeptide hydrogel loaded with PEDOT microparticles, further interconnected through an additional semi-interpenetrated PEDOT network formed by electropolymerization, displayed a specific capacitance of 45.4 ± 0.7 mF cm^{-2}.[44] In contrast, PEDOT electrodes coated with aromatic α-peptides exhibited areal specific capacitances several orders of magnitude lower than those achieved in the present study.[30]

Galvanostatic charge–discharge analysis. GCD curves (5 cycles) between 0.0 and 0.8 V were run at different current intensities. Fig. 8a and b show representative GCD curves for 2PEDOT(3m) and 2PEDOT(3m)-**TFA·DP1** electrodes. For both electrodes, the shape of the curves deviated from the ideal triangular shape, evidencing that the slow charge step was followed by a very fast discharge step. The decrease in the area of the plot with increasing intensities was attributed to the redox reaction that took place at the electrode/electrolyte interface. The symmetry of the charge–discharge process is usually measured by the coulombic efficiency (η, eqn (3)), which was evaluated as the ratio between the discharging and charging times (t_d and t_c, respectively) for the electrochemical window between 0.0 V and 0.8 V. For both electrodes, η was kept below 16%, independently of the intensity, suggesting that the internal resistance of the electrodes themselves consumes the most electrical discharge energy.

The GCD curves recorded for 2PEDOT(15s) (Fig. 8c) showed important differences with respect to those obtained for 2PEDOT(3m) and 2PEDOT(3m)-**TFA·DP1**. First, the reached voltage increased with the current intensity, while the charging time was significantly high (*i.e.* between 3 and 10 s depending on the current intensity). These features indicated that the flow of electrons from the first to the second layer is not continuous, affecting both the charging time and the reached voltage. Second, a significant voltage drop (V_{drop}) appeared at the beginning of the discharging process. This effect, which increased with the current intensity from V_{drop} = 0.11 V at 0.058 mA to V_{drop} = 0.58 V at 0.66 mA, was attributed to the electrode interfacial resistance to charge transport, which affected the current flow.

Finally, the GCD curves obtained for 2PEDOT(15s)-**TFA·DP1** (Fig. 8d) show improvements with respect to those of the rest of the systems. First, the cell voltage was 0.8 V for all tested current intensities, including the lowest one. Furthermore, the voltage drop was significantly lower than that observed for 2PEDOT(15s), improving the shape of the curves. Most importantly, the coulombic efficiency was significantly tuned by decreasing the current intensity, which was due to the charging time that was lower for 2PEDOT(15s)-**TFA·DP1** than for the other systems. For example, at a current intensity of 0.22 mA, t_c was 2.15 and 0.54 s for 2PEDOT(3m) and 2PEDOT(15s)-**TFA·DP1**, respectively (Fig. 8a and d). The behavior of t_c allowed the latter to achieve a η of 25% when the applied current intensity was 0.05 mA only (with t_d and t_c of 0.56 and 2.22 s, respectively). Instead, for 2PEDOT(3m), t_c increased much more than t_d when the applied current was lower than 0.22 mA, leading to η lower than 13%.

Electrochemical impedance spectroscopy. EIS was employed to investigate the electrical resistance. The recorded Nyquist plots (Fig. 9a-b), in which the negative imaginary impedance $-Z''$ was plotted *versus* the real part of the impedance Z', showed a semicircle in all cases. The starting point of each curve (*i.e.* the intercept of the curve with the real *Z*-axis in the high frequency region) indicated the resistance of the electrolytic medium (R_S). R_S only depends on the ionic concentration, type of ions, temperature and the geometry of the area in which the current is applied. Considering that in this work assays were performed using 0.1 M $LiClO_4$ acetonitrile solution and that the temperature was very similar in all experiments, the small variation expected among the different analyzed systems

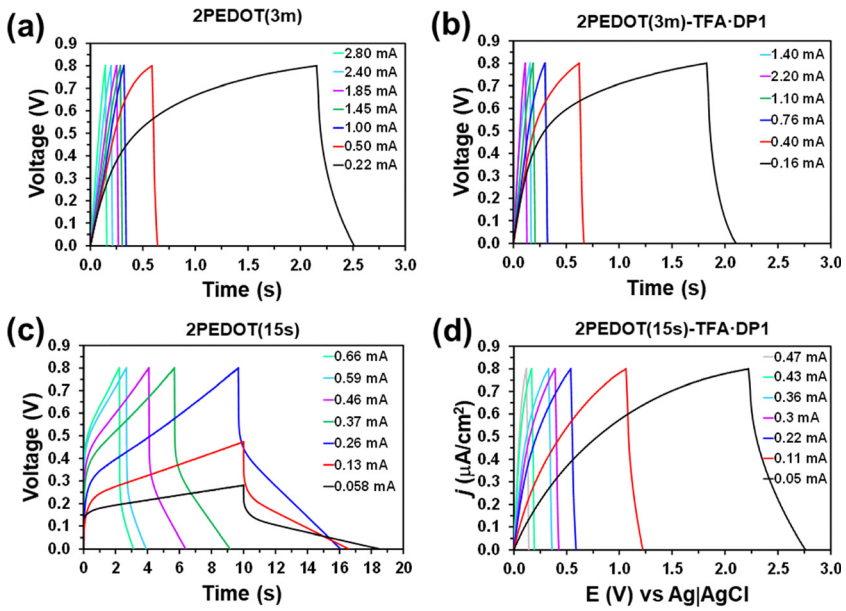

Fig. 8 Representative GCD curves for (a) 2PEDOT(3m), (b) 2PEDOT(3m)-**TFA·DP1**, (c) 2PEDOT(15s) and (d) 2PEDOT(15s)-**TFA·DP1**.

should be attributed to the morphology (*i.e.* geometry) of the electrodes. Thus, the lower the ion mobility (*i.e.* more restricted by the morphology) in the electrode, the higher the R_S value will be. As can be seen in Fig. 9c, the R_S values obtained for the four systems were of the same order of magnitude. However, independently of t_p, the **TFA·DP1**-containing devices showed higher R_S values than those without peptide. This was attributed to the electrostatic repulsions between the TFA anions used to stabilize the peptide at the intermediate layer and ClO_4^- counteranions, which restricted diffusion and the mobility of the latter into the polymeric matrix.

The diameter of the semicircle corresponded to the charge transfer resistance (R_P) at the electrode/electrolyte interface, also known as the interface reaction resistance. Independently of the t_p, the R_P, which included the effects induced by the multilayered configuration of the electrodes, was significantly lower for the peptide-containing electrodes than for those without peptide (Fig. 9d). The R_P values obtained for 2PEDOT(3m) and 2PEDOT(3m)-**TFA·DP1** were 69.3 and 10.7 Ω cm^{-1}, respectively, while those of 2PEDOT(15s) and 2PEDOT(15s)-**TFA·DP1** were 45.8 and 1.0 Ω cm^{-1}, respectively. This indicated that peptide-containing electrodes presented better interfacial contact with the electrolyte, which enhanced the ion transport and reduced the interfacial resistance. On the other hand, the lower resistance of the electrodes prepared using t_p = 15 s in relation to those obtained using 3 min was totally consistent with our previous observations. Thus, our results showed that the smaller the thickness of the films, the more favorable the peptide-induced reorganization of the capacitive and conductive paths is.

Overall, the performance of SCs based on 2PEDOT(15s)-**TFA·DP1** electrodes was intermediate between those reported for devices prepared using 3-layered electrodes with poly(*N*-methylpyrrole) (PNMPy)[18] and clays[16] at the intermediate layer (hereafter referred to as 2PEDOT-PNMPy and 2PEDOT-clay, respectively) instead of **TFA·DP1** assemblies. The performance of 2PEDOT-PNMPy, which improved by decreasing the t_p, as in this work, was attributed to a synergistic effect produced by the favorable interaction between the PEDOT and PNMPy layers at the corresponding interfaces, with the PNMPy intermediate sheet promoting the dielectric breakage effect (*i.e.* the electrical conductivity was ~10^5 S cm^{-1} higher for PEDOT than for PNMPy).[18,45] Instead, the very low performance of SCs based on 3-layered 2PEDOT-clay electrodes was attributed to the completely inert electrochemical nature of the clays.[46] The electrochemical response of **TFA·DP1** assemblies was primarily due to electron transport between stacked rings (*i.e.* intermolecular electronic contribution) and the movement of ions that stabilize the amine. This response was lower than that of PNMPy in which the charge moved along the polymer molecules both at the electronic level (intramolecular delocalization of polarons and bipolarons) and at the ionic level (counterions that neutralize the charge of the PNMPy chains). In the case of clays, the ions were strongly trapped between the charged silicate layers, and consequently, these materials did not exhibit electrochemical response.

On the other hand, it is worth noting that the use of electro-responsive peptide assemblies could be readily extended to the fabrication of various types of asymmetric supercapacitors. This could be achieved either by employing different conducting polymers at each electrode while using the same peptide in both, or by using different assembled peptides at each electrode while keeping the conducting polymer identical. Furthermore, **TFA·DP1** peptide assemblies could also be integrated into flexible supercapacitors based on conducting polymer hydrogels. This could be accomplished either by incorporating pre-formed **TFA·DP1** assemblies during the gelation process or

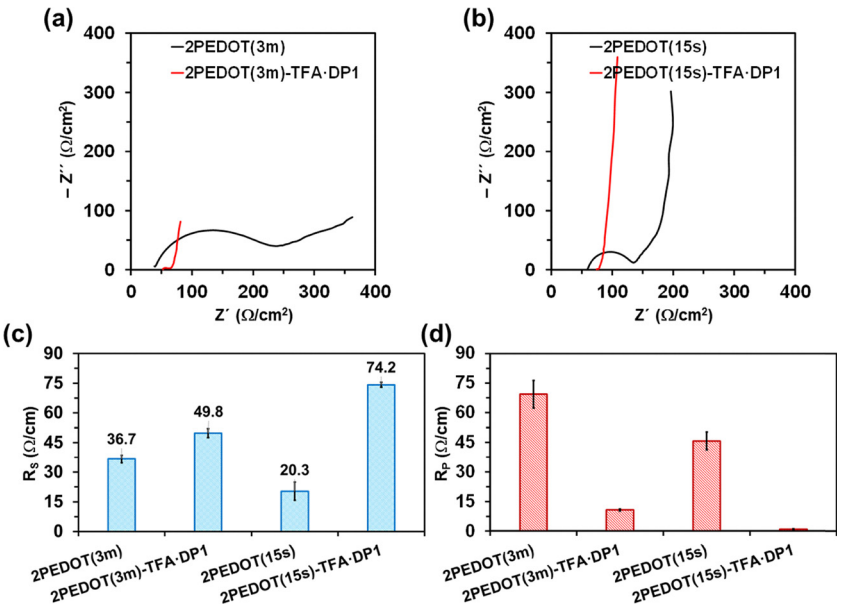

Fig. 9 Nyquist plots recorded for SCs prepared using: (a) 2PEDOT(3m) and 2PEDOT(3m)-**TFA·DP1**; and (b) 2PEDOT(15s) and 2PEDOT(15s)-**TFA·DP1**. (c) R_S and (d) R_P values derived from EIS data.

by promoting the formation of peptide assemblies within a preformed 3D hydrogel network (*i.e.* infiltrating the peptide into the hydrogel).

Conclusions

In summary, we demonstrated that small α/β-dipeptides **DP1** and **TFA·DP1** can self-assemble into well-ordered structures on electropolymerized PEDOT substrates. In this novel self-assembly approach, in which the organization of the peptide molecules is conditioned by the very high roughness and particular morphology of such a conducting polymer, a synergy between the semi-conductive substrate and the self-assembled structures was sought in the electrochemical response. In order to prove such synergy, we systematically studied the electrochemical behavior of 3-layered electrodes consisting of two PEDOT layers separated by an intermediate layer of one of the self-assembled peptides constructed for the first time. Furthermore, the influence of the PEDOT layer thickness was taken into account, considering polymerization times of 3 min and 15 s. Electrochemical evaluation of the resulting electrodes revealed that the synergy between PEDOT and the self-assembled peptide only occurred with **TFA·DP1**. This was attributed to the fact that such a peptide, when forming ordered structures, not only transported electrons through the stacked aromatic rings, but also the counterions associated with the charged amino terminal group.

Symmetric SCs prepared using 2PEDOT(3m)-**TFA·DP1** and 2PEDOT(15s)-**TFA·DP1** were characterized and compared with those obtained using electrodes without peptide at the intermediate layer. Peptide-containing systems not only displayed lower electrical resistance but also good voltammetric response and charge–discharge capacity. Our results suggest that self-assembled peptide nano- and micro-structured materials can perform excellently as biocompatible active components in electrochemical SCs, which are promising for use in wearable, implantable, and biodegradable devices. The proof of concept reported in the present study could be extended to *de novo* designed peptide sequences. We therefore envision that molecular engineering aimed, on the one hand, to having sequences that promote electronic and ionic transport efficiently, and on the other hand, to facilitate obtaining ordered self-assembled structures on soft semi-conducting substrates, will have broad and important applications in bioelectronics.

Conflicts of interest

There are no conflicts to declare.

Data availability

The data supporting the findings of this study have been included in the article and its supplementary information (SI). Supplementary information is available. See DOI: https://doi.org/10.1039/d5ma01170a.

Other datasets generated during this study, such as raw and processed data, are available from the corresponding author upon reasonable request.

Acknowledgements

This publication received funding from the European Union's research and innovation program under the Marie Skłodowska-Curie grant agreement No. 101072645. The IMEM-BRT group thanks the Agència de Gestió d'Ajuts Universitaris i de Recerca (2021 SGR 00387) for financial support. This work is part of Maria de Maeztu Units of Excellence Programme CEX2023-001300-M funded by MCIN/AEI/10.13039/501100011033. Support for the research of C. A. was also received through the prize ''ICREA Academia 2022'' for excellence in research funded by the Generalitat de Catalunya.

References

1 X. Fan, C. Zhong, J. Liu, J. Ding, Y. Deng, X. Han, L. Zhang, W. Hu, D. P. Wilkinson and J. Zhang, *Chem. Rev.*, 2022, **122**, 17155–17239.
2 Y. Jia, J. Zhang, D. Kong, C. Zhang, D. Han, J. Han, Y. Tao, W. Lv and Q.-H. Yang, *Adv. Funct. Mater.*, 2022, **32**, 2204272.
3 L. Liu, X. Zhang, Y. Liu and X. Gong, *ACS Appl. Electr. Mater.*, 2025, **7**, 2233–2270.
4 S. Zhang, Y. Liu, J. Hao, G. G. Wallace, S. Beirne and J. Chen, *Adv. Funct. Mater.*, 2022, **32**, 2103092.
5 J. Chen and P. S. Lee, *Adv. Energy Mater.*, 2021, **11**, 2003311.
6 L. Li, J. Meng, M. Zhang, T. Liu and C. Zhang, *Chem. Commun.*, 2022, **58**, 185–207.
7 H. A. Khan, M. Tawalbeh, B. Aljawrneh, W. Abuwatfa, A. Al-Othman, H. Sadeghifar and A. G. Olabi, *Energy*, 2024, **295**, 131043.
8 C. Padwal, H. D. Pham, L. T. My Hoang, S. Mundree, A. K. Nanjundan, S. G. Krishnan and D. Dubal, *ChemSusChem*, 2024, **17**, e202301866.
9 S. S. Shah, F. Niaz, M. A. Ehsan, H. T. Das, M. Younas, A. S. Khan, H. U. Rahman, S. M. A. Nayem, Md. M. Oyama and A. Aziz, *J. Energy Storage*, 2024, **79**, 110152.
10 Y. Yu, C. Yang, Y. Jiang, J. Zhu, Y. Zhao, S. Liang, K. Wang, Y. Zhou, Y. Liu and J. Zhang, *Small*, 2023, **19**, 2303779.
11 A. M. Bryan, L. M. Santino, Y. Lu, S. Acharya and J. M. D'Arcy, *Chem. Mater.*, 2016, **28**, 5989–5998.
12 C. Bauer, M. Kirchner and A. Krueger, *Energy Adv.*, 2024, **3**, 1422–1430.
13 M. N. Gueye, A. Carella, J. Faure-Vincent, R. Demadrille and J.-P. Simonato, *Prog. Mater. Sci.*, 2020, **108**, 100616.
14 M. G. Tadesse, N. Simon and J. F. Lübben, *Adv. Energy Sustainability Res.*, 2024, **5**, 2400006.
15 X. Wang, P. Wang, W. Tian, H. Bu and K. Zhang, *ACS Sustainable Chem. Eng.*, 2023, **11**, 17510–17518.
16 D. Aradilla, D. Azambuja, F. Estrany, M. T. Casas, C. A. Ferreira and C. Alemán, *J. Mater. Chem.*, 2012, **22**, 13110–13122.

17 F. Niu, X. Han, H. Sun, Q. Li, X. He, Z. Liu, J. Sun and Z. Lei, *ACS Sustainable Chem. Eng.*, 2021, **9**, 4146–4156.
18 D. Aradilla, F. Estrany and C. Alemán, *J. Phys. Chem. C*, 2011, **115**, 8430–8438.
19 W. Yan, J. Li, G. Zhang, L. Wang and D. Ho, *J. Mater. Chem. A*, 2020, **8**, 554–564.
20 M. F. Jimoh, G. S. Carson, M. B. Anderson, M. F. El-Kady and R. B. Kaner, *Adv. Funct. Mater.*, 2025, **35**, 2405569.
21 T. Cheng, X. L. Yang, S. Yang, L. Li, Z. T. Liu, J. Qu, C. F. Meng, X. C. Li, Y. Z. Zhang and W. Y. Lai, *Adv. Funct. Mater.*, 2022, **33**, 2210997.
22 X. Liu, Y. Chen, H. Zhang, L. Zhuo, Q. Huang, W. Zhang, H. Chen and Q. Ling, *J. Colloid Interface Sci.*, 2024, **660**, 735–745.
23 P. Gomez-Romero, *Adv. Mater.*, 2001, **13**, 163–174.
24 S. Chakraborty, K. El Battioui and T. Beke-Somfai, *Small Sci.*, 2024, **4**, 2300217.
25 K. Hu, C. Zheng, X. Miao and L. Wang, *J. Mater. Chem.*, 2018, **6**, 8047–8052.
26 Y. Tian, J. Li, A. Wang, Q. Li, H. Jian and S. Bai, *Macromol. Biosci.*, 2023, **23**, 2300171.
27 O. S. Tiwari, *Mol. Syst. Des. Eng.*, 2022, **7**, 171–181.
28 J. Zhao, Q. Liu, X. Tong, Y. Wang, K. Cai and W. Ji, *Adv. Funct. Mater.*, 2024, **34**, 2401466.
29 M. R. Biradar, H. A. Mirgane, S. V. Bhosale and S. V. Bhosale, *J. Energy Chem.*, 2024, **99**, 253–276.
30 A. Fontana-Escartín, E. Rosa, C. Diaferia, S. Lanzalaco, A. Accardo and C. Alemán, *J. Colloid Interface Sci.*, 2025, **679**, 441–454.
31 Y. Wang, K. Wan, C. Liu and W. Zhang, In Peptide Nanomaterials for Energy and Environmental Science Applications, *Peptide Nano-Chemistry and Nanotechnology*, ed G. Wei, Springer, Singapore, 2025.
32 K. Hu, C. Zheng, M. An, X. Ma and L. Wang, *J. Mater. Chem. A*, 2018, **6**, 8047–8052.
33 R. Bucci, A. Contini, F. Clerici, E. M. Beccalli, F. Formaggio, I. Maffucci, S. Pellegrino and M. L. Gelmi, *Front. Chem.*, 2019, **7**, 192.
34 R. P. Cheng, S. H. Gellman and W. F. DeGrado, *Chem. Rev.*, 2001, **101**, 3219–3232.
35 A. Bonetti, S. Pellegrino, P. Das, S. Yuran, R. Bucci, N. Ferri, F. Meneghetti, C. Castellano, M. Reches and M. L. Gelmi, *Org. Lett.*, 2015, **17**, 4468–4471.
36 R. Bucci, P. Das, F. Iannuzzi, M. Feligioni, R. Gandolfi, M. L. Gelmi, M. Reches and S. Pellegrino, *Org. Biomol. Chem.*, 2017, **15**, 6773–6779.
37 M. Gul, D. A. Quintana-Romero, A. Fontana-Escartín, M. L. Gelmi, M. M. Pérez-Madrigal, E. Chiesa, R. Bucci and C. Alemán, *Adv. Mater. Interfaces*, 2025, e00254.
38 Y. Zhang, L. Li and B. He, *RSC Adv.*, 2024, **14**, 30045–30054.
39 E. Poverenov, M. Li, A. Bitler and M. Bendikov, *Chem. Mater.*, 2010, **22**, 4019–4025.
40 K. Shezad, K. J. Zhang, M. Hussain, H. Dong, C. X. He, X. J. Gong, X. L. Xie, J. T. Zhu and L. Shen, *Langmuir*, 2016, **32**, 8238–8244.
41 D. Aradilla, M. M. Pérez-Madrigal, F. Estrany, D. Azambuja, J. I. Iribarren and C. Alemán, *Org. Electr.*, 2013, **14**, 1483–1495.
42 D. Amoura, M. Sánchez-Jiménez, F. Estrany, L. Makhloufi and C. Alemán, *Eur. Polym. J.*, 2015, **69**, 296–307.
43 I. O. Oladele, S. O. Adelani, A. S. Taiwo, I. M. Akinbamiyorin, O. F. Alanrewaju and A. O. Orisawayi, *RSC Adv.*, 2025, **15**, 7509–7534.
44 M. C. G. Saborío, S. Lanzalaco, G. Fabregat, J. Puiggalí, F. Estrany and C. Alemán, *J. Phys. Chem. C*, 2018, **122**, 1078–1090.
45 F. Estrany, D. Aradilla, R. Oliver, E. Armelin and C. Aleman, *Eur. Polym. J.*, 2008, **44**, 1323–1330.
46 N. Borras, F. Estrany and C. Alemán, *Org. Electr.*, 2017, **51**, 322–331.